Transmission and reflection of three-dimensional Boussinesq internal gravity wave packets in nonuniform retrograde shear flow

Alain D. Gervais [1,*] Gordon E. Swaters,[1] and Bruce R. Sutherland [2,3]

[1]*Department of Mathematical and Statistical Sciences, University of Alberta,*
Edmonton, Alberta, Canada T6G 2G1
[2]*Department of Earth and Atmospheric Sciences, University of Alberta,*
Edmonton, Alberta, Canada T6G 2E3
[3]*Department of Physics, University of Alberta, Edmonton, Alberta, Canada T6G 2E1*

The transmission and reflection of finite-amplitude, three-dimensional, internal gravity wave packets across a reflection level are examined numerically in a Boussinesq fluid with a nonuniform retrograde shear flow. We derive the critical amplitude for wave packets to transmit partially above the reflection level predicted by linear theory, occurring when the magnitude of the vertical shear associated with their wave-induced mean flow is locally greater than that of the background shear. We find that transmitted and reflected wave packets corresponding to strongly nonhydrostatic primary waves can interact resonantly to generate quadratically nonlinear secondary wave packets. We propose a weakly nonlinear mechanism, based on self-induced local decreases in buoyancy, to explain the generation of secondary wave packets by nonbreaking moderately nonhydrostatic primary waves, and we predict the critical amplitude for its onset. Numerical simulations are performed for a range of nonhydrostatic wave packets with small to moderately large initial amplitudes with their predicted wave-induced mean flow superimposed. Transmission is quantified using the pseudomomentum corresponding to upward-propagating waves above the reflection level predicted by linear theory. In most cases, the transmission transiently grows and decays as wave packets first cross and then reflect from the reflection level predicted by linear theory. We find that for all but the most strongly nonhydrostatic wave packets, larger-amplitude waves exhibit smaller peak transmission, relative to the total pseudomomentum. The time at which peak transmission occurs is diagnosed. Strongly nonhydrostatic wave packets exhibit continuous transmission well above the reflection level. When we consider the time interval for transmission to decrease to half its peak value, we find that this becomes longer with larger initial amplitude. These behaviors are found to result from the combined effects of modulational instability and the generation and evolution of secondary wave packets. Results are discussed in the context of previous studies of one- and two-dimensional wave-packet transmission and reflection.

I. INTRODUCTION

Internal gravity waves propagate horizontally and vertically within stably stratified fluids, such as the oceans and atmosphere. They represent an important mechanism for transporting energy and momentum across a broad range of spatial scales within these fluids (see, e.g., Refs. [1,2]). Wave propagation is influenced by environmental factors such as rotation and nonuniform stratification

---

*adgervai@ualberta.ca

and background flow, and by nonlinear interactions between the waves themselves [3]. Among these, in this study we are interested in the combined linear influence of nonuniform background flow and the nonlinear interaction between moderately large-amplitude quasimonochromatic wave packets and their wave-induced mean flow.

In the ocean, internal gravity waves are generated, e.g., by surface wind stress and periodic tidal flow over bathymetry (see, e.g., Ref. [4]), and as nonhydrostatic lee waves by quasisteady flows such as the Antarctic Circumpolar Current through the Drake Passage [5]. Upward-propagating atmospheric internal gravity waves are generated by several mechanisms, including flow over orography (see, e.g., Ref. [6], Sec. 6), and at the tropopause by convective processes such as overshooting convection from supercell thunderstorms [7,8] and tropical cyclones [9]. In both the atmosphere and ocean, the structure of the background flow is but one factor determining whether the variously generated waves dissipate locally, or continue propagating ultimately to deposit their energy and momentum far from their source (see, e.g., Refs. [4,10,11]).

A steady nonuniform background shear flow that depends on height alone acts to Doppler-shift the wave frequency. Linear theory (see Ref. [12]) predicts that shifting toward higher frequencies corresponds to waves with progressively vertically oriented phase lines, so that the waves ultimately reach a "reflection level" at the height where their Doppler-shifted frequency is equal to the local background buoyancy frequency.

Even in the absence of an existing background flow, moderately large-amplitude wave packets induce an order amplitude-squared mean Eulerian flow that locally accelerates the fluid and interacts nonlinearly with the wave packet [13,14]. The character of the induced mean flow, hence the nature of the nonlinear interaction, depends on whether the wave packet is one-, two-, or three-dimensional. One-dimensional wave packets that are horizontally periodic and vertically localized induce a unidirectional, horizontally uniform, vertically localized mean flow that translates vertically with the wave packet at the group speed. This mean flow, arising from the vertical divergence of momentum flux, was derived using conservation of momentum for quasimonochromatic wave packets (see Ref. [12]), and it is equivalent to the pseudomomentum per unit mass of plane internal waves [14,15]. Two-dimensional wave packets without rotation similarly induce a mean flow, manifest as hydrostatic long waves that radiate below and horizontally outward far from an upward-propagating wave packet [16,17]. Fully localized three-dimensional wave packets again induce a qualitatively distinct mean flow—generally known as the "Bretherton flow"—which is unidirectional in the vertical through the center of the wave packet, but having a dipole structure in the horizontal [13,18,19].

Interactions between a wave packet and its induced mean flow drive a range of instability mechanisms, among which self-acceleration and modulational instability are of particular relevance to this study. Somewhat heuristically, Sutherland [20] proposed that a wave packet was prone to self-acceleration if its maximum wave-induced mean flow was greater than its streamwise group speed. Under this assumption, a critical amplitude for the onset of this instability was derived for one- and two-dimensional wave packets [20] and for three-dimensional wave packets with rotation [19]. Results of numerical simulations agreed well with this heuristic condition for one-, but not two- or three-dimensional wave packets, which destabilized and ultimately overturned even with initial amplitudes well below those predicted for self-acceleration. Crucially, this imposes a practical upper bound on the initial amplitudes used in this study: We are interested in the transmission and reflection of small- and moderately large-amplitude wave packets, but not so large that the waves overturn due to self-acceleration.

Unlike self-acceleration instability, there is no minimum amplitude for the onset of modulational instability. This instability acts through the weakly nonlinear dispersion relation to locally Doppler-shift the wave frequency, resulting in a local change to the group velocity. A local decrease (increase) in any component of the group velocity causes the extent of the wave packet to narrow (broaden) in that direction and its amplitude to grow (decay) [21,22]. In one dimension, the transition between modulationally stable and unstable wave packets occurs for those with absolute vertical wave number relative to the horizontal wave number of approximately $2^{-1/2}$, thus corresponding to waves

with the fastest vertical group speed. Conversely, two-dimensional wave packets are always unstable to modulations, though dominantly in the vertical [17,23]. In the two-dimensional case, the induced long waves change sign from positive to negative across the vertical extent of the wave packet [17,24]. Three-dimensional wave packets were found by Gervais *et al.* [19] to exhibit the same modulational stability properties in the vertical as their one-dimensional counterparts because their respective induced mean flows have an analogous unidirectional vertical structure.

Studies investigating the relationship between internal waves and mean flows have typically considered the isolated case of either the interactions between waves and an existing background flow (see, e.g., Refs. [25–33]), or between waves and their induced mean flow in an otherwise stationary fluid (see, e.g., Refs. [17,19,20,24,34–36]). Relatively few studies (see, e.g., Refs. [37–39]) have examined in detail the nonlinear evolution of a moderately large-amplitude wave packet as it interacts with both its induced mean flow and an existing nonuniform background flow. Using ray theory, Robinson [37] predicted the trajectory of a one-dimensional wave packet with its induced mean flow superimposed, propagating in an existing linear shear flow. In particular, the Doppler-shifted frequency predicted by linear theory was modified to itself be Doppler-shifted by the induced mean flow. The idealized analysis suggested the competing effects of the oppositely signed background, and induced mean flows allowed the waves to propagate higher before reflecting than without the influence of the induced mean flow. Consequently, the reflection time was delayed. These results were more pronounced as amplitude increased, due to the magnitude of the induced mean flow increasing quadratically with amplitude. Sutherland [38] performed fully nonlinear simulations of small- and moderately large-amplitude one- and two-dimensional nonhydrostatic wave packets in uniform retrograde shear flow. Wave packets with sufficiently large initial amplitude were able to propagate well above the reflection level predicted by linear theory provided the magnitude of the vertical shear associated with the wave-induced mean flow was somewhere greater than that of the background shear. The superimposed background and wave-induced shears, being locally equal and opposite, allowed a wave packet to propagate as if the background flow was effectively uniform in the vicinity of the advancing wave packet. The present study differs from those of [37,38] in that we combine ray theory and numerical simulations to examine fully localized three-dimensional wave packets with amplitude envelopes that are Gaussian in all three spatial dimensions, in a nonuniform background flow that transitions smoothly with height from stationary to linearly decreasing.

The paper is laid out as follows. In Sec. II we review the theory of linear (i.e., small-amplitude) wave-packet propagation in nonuniform background flow, we derive the critical amplitude for wave-packet penetration above the reflection level, we describe secondary wave generation by triadic resonant instability and our "self-reflection" mechanism, and we define a transmission coefficient. The fully nonlinear code is described in Sec. III. The results of numerical simulations are described and compared with theoretical predictions in Sec. IV. In Sec. V we discuss our results and offer concluding remarks.

II. THEORY

We first review the equations of ray theory that describe the trajectory of a small-amplitude wave packet as it propagates in a nonuniform background flow, providing predictions for the height and time at which a small-amplitude wave packet is anticipated to reflect. We then describe how the wave-induced Eulerian mean flow is anticipated to modify the linear behavior of moderately large-amplitude wave packets to motivate our derivation of the critical amplitude for which wave-packet penetration well above the predicted reflection level occurs. Using weakly nonlinear theory, we then derive the critical amplitude for secondary wave generation. The section concludes with the definition of an appropriate transmission coefficient.

A. Linear theory

In a uniformly stratified, nonrotating, inviscid Boussinesq fluid that is stationary in the absence of waves, plane internal gravity waves propagate in the *xz*-plane with intrinsic frequency

$\omega_0 = N_0 k_0 / \sqrt{k_0^2 + m_0^2}$, with phase lines oriented at the angle $\Theta_0 = \tan^{-1} |m_0/k_0|$ to the vertical, in which $k_0 > 0$ and m_0 are the streamwise and vertical wave numbers, respectively. We assume the fluid is uniformly stratified so that the background buoyancy frequency $N_0 = \sqrt{-(g/\rho_0)d\bar{\rho}/dz}$ is constant, in which g is the acceleration of gravity, ρ_0 is a constant reference density, and $d\bar{\rho}/dz$ is the background density gradient [12,14]. In the absence of a background flow, an initially upward- and rightward-propagating small-amplitude wave packet will propagate along a linear path in the direction Θ_0 to the vertical.

A wave packet is a localized oscillatory disturbance, having vertical displacement ξ, of the form

$$\xi(\mathbf{x}, t) = \tfrac{1}{2} A_\xi(\mathbf{x}, t) e^{i\varphi_0} + \text{c.c.}, \tag{1}$$

in which the phase is $\varphi_0 = \mathbf{k}_0 \cdot \mathbf{x} - \omega_0 t$, where $\mathbf{k}_0 = (k_0, 0, m_0)$ is the wave-number vector, $\mathbf{x} = (x, y, z)$, the (possibly complex valued) amplitude envelope is $A_\xi(\mathbf{x}, t)$, and c.c. denotes the complex conjugate. Using (1), waves are oriented in the xz-plane, but A_ξ can vary in y. For a quasimonochromatic wave packet, A_ξ varies slowly in $\mathbf{x}$ and t compared with wavelength and period.

A nonuniform background flow $\bar{u}(z)$ acts to Doppler-shift the intrinsic frequency ω_0, with the resulting Doppler-shifted frequency being

$$\Omega = \omega_0 - k_0 \bar{u}. \tag{2}$$

The path of a small-amplitude wave packet from an initial position $(x_0, 0, z_0)$ through a uniformly stratified Boussinesq fluid is predicted using ray theory (see, e.g., Ref. [12], Sec. 6.5). Provided $\bar{u}$ does not change significantly over a vertical wavelength, conforming with the implicit use of the WKBJ approximation, the path $(x(t), 0, z(t))$ traced by the centroid of a small-amplitude wave packet is described by the solution of the differential equations

$$\frac{dx}{dt} = c_{gx}(m(z)) + \bar{u}(z), \tag{3}$$

$$\frac{dz}{dt} = c_{gz}(m(z)), \tag{4}$$

where the group velocity is given by $\mathbf{c}_g = (c_{gx}, 0, c_{gz}) = m N_0 \|\mathbf{k}\|^{-3} (m, 0, -k_0)$, in which $\|\mathbf{k}\| = (k_0^2 + m^2)^{1/2}$ and k_0 is constant. An expression for the vertical wave number $m = m(z)$ is found by equating the expression for the Doppler-shifted frequency (2) to the local intrinsic frequency [31], yielding the auxiliary equation

$$m = m(z(t)) = \text{sgn}(m) k_0 \sqrt{\frac{N_0^2}{\Omega^2(z(t))} - 1}, \tag{5}$$

where $\text{sgn}(m) = -1$ and 1 if the wave packet is propagating, respectively, upward ($c_{gz} > 0$) and downward ($c_{gz} < 0$).

An initially upward-propagating small-amplitude wave packet [i.e., one with $k_0 > 0$ fixed and $m(z(t_0)) = m_0 < 0$] is anticipated to reflect at the height z_r at which $\Omega = N_0$. In practice, for steady background flows that are nonuniform with height, Eqs. (3) and (4) cannot be solved analytically, and the reflection level must instead be diagnosed from the numerical solution of (4). The reflection level corresponds to the height at which $m(z_r) = 0$. The reflection time, t_r, is the time at which $z(t) = z_r$.

B. Wave-induced mean flow and reflection level penetration

As a moderately large-amplitude fully localized three-dimensional wave packet propagates, wave-wave interactions on the scale of the wave packet induce an order amplitude-squared mean flow—the Bretherton flow—which locally accelerates the fluid in the vicinity of the wave packet. In the absence of a background flow, the horizontal components of the Bretherton flow are given

initially by the Fourier integral [18,24,40]

$$\begin{bmatrix} u_{\mathrm{BF}} \\ v_{\mathrm{BF}} \end{bmatrix} = \frac{1}{2} N_0 \|\mathbf{k}_0\| \int_{\mathbb{R}^3} \frac{\lambda}{\kappa^2 + \lambda^2} \begin{bmatrix} \lambda \\ -\kappa \end{bmatrix} \widehat{|A|^2} e^{i\boldsymbol{\kappa} \cdot (\mathbf{x} - \mathbf{x}_0)} d\kappa \, d\lambda \, d\mu, \tag{6}$$

where $\widehat{|A|^2} = (2\pi)^{-3} \int_{\mathbb{R}^3} |A(\mathbf{x})|^2 e^{-i\boldsymbol{\kappa} \cdot (\mathbf{x} - \mathbf{x}_0)} dx \, dy \, dz$ is the Fourier-transformed squared modulus of the vertical displacement amplitude envelope A_ξ, in which we have defined $A \equiv A_\xi$ for convenience, and $\boldsymbol{\kappa} = (\kappa, \lambda, \mu)$ is the vector of transform variables.

In the study of one- and two-dimensional wave-packet transmission in uniformly stratified and sheared flow, Sutherland [38] found that rather than displacing a reflection level as predicted by [37], a wave packet could transmit partially through the predicted reflection level provided the magnitude of the vertical shear associated with the wave-induced mean flow was locally greater than that of the background shear, $|s|$. For three-dimensional wave packets, whose induced mean flow is the Bretherton flow, this penetration condition is given explicitly by

$$\left| \frac{\partial u_{\mathrm{BF}}}{\partial z} \right| > |s|. \tag{7}$$

For example, we consider solutions of this inequality for a trivariate Gaussian wave packet with initial amplitude envelope

$$A = A_0 \mathcal{A} = A_0 \exp\left[-\frac{1}{2} \left(\frac{x^2}{\sigma_x^2} + \frac{y^2}{\sigma_y^2} + \frac{(z - z_0)^2}{\sigma_z^2} \right) \right], \tag{8}$$

where the constant A_0 is the peak vertical displacement, and σ_x, σ_y, and σ_z are the streamwise, spanwise, and vertical extents, respectively, of the wave packet. Squaring and Fourier transforming (8) gives

$$\widehat{|A|^2} = \frac{1}{8\pi^{3/2}} \sigma_x \sigma_y \sigma_z A_0^2 \exp\left[-\left(\sigma_x^2 \kappa^2 + \sigma_y^2 \lambda^2 + \sigma_z^2 \mu^2 \right)/4 \right]. \tag{9}$$

Using (9) in (6), it follows that, at a given height, the largest value of $|u_{\mathrm{BF}}|$, hence also that of $|\partial u_{\mathrm{BF}}/\partial z|$ in (7), is aligned with the horizontal center of the wave packet. Accordingly, setting $\mathbf{x} = (0, 0, z)$ in the streamwise component of (6) yields an analytically tractable integral expression for a vertical profile of $|u_{\mathrm{BF}}|$ [14,18]:

$$\max_{x,y}\{u_{\mathrm{BF}}\} = u_{\mathrm{BF}}(0, 0, z, t = 0) = \frac{1}{2} N_0 \|\mathbf{k}_0\| \frac{A_0^2}{R_y + 1} e^{-(z - z_0)^2/\sigma_z^2}, \tag{10}$$

where $R_y = \sigma_y/\sigma_x$ is the spanwise aspect ratio of the wave packet. Differentiating (10) with respect to z, it is straightforward to show that the maximum wave-induced shear occurs at $z - z_0 = -\sigma_z/\sqrt{2}$, with corresponding maximum

$$\frac{1}{R_y + 1} \frac{N_0 \|\mathbf{k}\|}{\sqrt{2e}\sigma_z} A_0^2.$$

Substituting this into the penetration condition (7) yields the critical vertical displacement amplitude, A_{RP}, above which a Gaussian wave packet is predicted to transmit partially through a reflection level:

$$A_{\mathrm{RP}} = \sqrt{\frac{\sigma_z (R_y + 1)\sqrt{2e}}{\|\mathbf{k}_0\|} \frac{|s|}{N_0}}. \tag{11}$$

This critical amplitude is plotted with $R_y = 1$ and $\sigma_z = 10k_0^{-1}$ for a range of absolute shear strength parameters $|s|/N_0$ in Fig. 1.

Another important parameter to consider is the critical amplitude at which waves are prone to self-acceleration. Extending the somewhat heuristic condition of Sutherland [20] from one- to three-dimensional wave packets with rotation, Gervais *et al.* [19] proposed that wave packets were prone
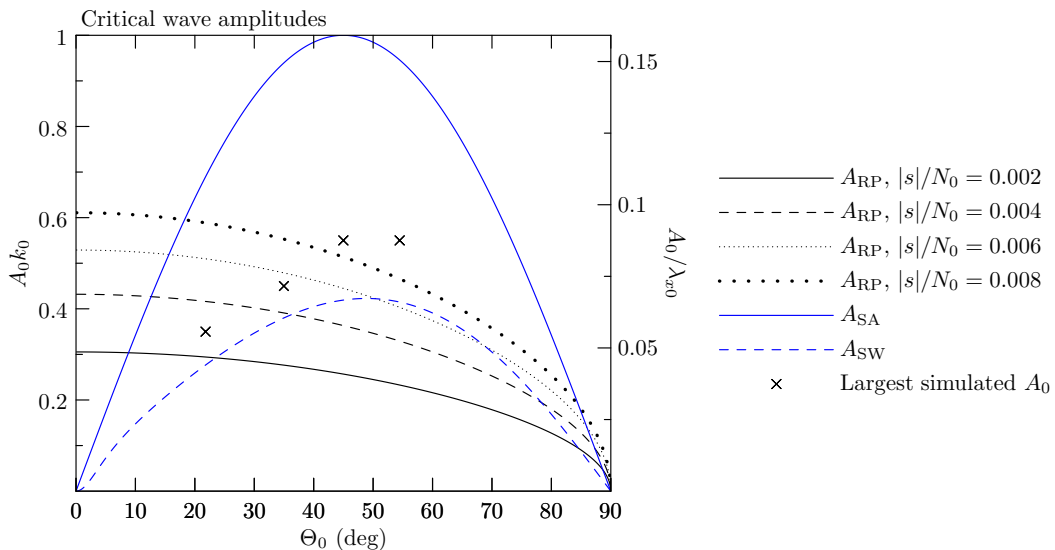
FIG. 1. Critical wave amplitudes for reflection level penetration $A_{\rm RP}$, given by (11), for a range of nondimensional absolute shear strength parameters $|s|/N_0$, instability due to self-acceleration $A_{\rm SA}$, given by (12), and for secondary wave generation $A_{\rm SW}$, given by (22). Crosses denote the largest initial amplitude used in simulations of wave packets with the corresponding $\Theta_0 = \tan^{-1} |m_0/k_0|$.

to self-acceleration instability if their maximum Bretherton flow was greater than their streamwise group speed. The critical amplitude [Ref. [19], equation (18) with Coriolis parameter $f_0 = 0$], was found to be

$$A_{\rm SA} = \frac{1}{\sqrt{2}k_0} \sin(2\Theta_0)\sqrt{R_y + 1}, \tag{12}$$

in which $\Theta_0 = \tan^{-1} |m_0/k_0|$. This critical amplitude is plotted with $R_y = 1$ as the solid blue curve in Fig. 1.

A wave packet is prone to overturning if it is of sufficiently large amplitude that the waves advect more dense fluid over less dense fluid. The approach to overturning is diagnosed by decreasing values of $\min\{N_T^2(\mathbf{x}, t)\}$ with time [19,20], where

$$N_T^2 \equiv N_0^2 + \Delta N^2 \tag{13}$$

is the "total" squared buoyancy frequency, in which $\Delta N^2 = -N_0^2 \partial\xi/\partial z$ is the local change in squared buoyancy due to waves. Overturning is diagnosed by the condition

$$\min\left\{N_T^2\right\} = 0. \tag{14}$$

This corresponds to the critical amplitude $A_{\rm OT} = 1/|m_0|$. For nonhydrostatic three-dimensional wave packets with $R_y = 1$, $A_{\rm OT} > A_{\rm SA}$. Consequently, $A_{\rm SA}$ is expected to limit the amplitude of waves that eventually overturn.

C. Secondary wave generation by nonbreaking primary waves

Existing studies examining secondary gravity wave generation have focused on their excitation resulting from primary wave breaking as observed in the middle and upper atmosphere [41–43] and from convectively and orographically generated three-dimensional primary waves in numerical simulations [44–48]. Secondary wave generation was modeled as a linear response to momentum

deposition by breaking waves [49–52]. We are unaware of any investigations of secondary wave-packet generation by nonbreaking primary waves. Our motivation to examine their generation mechanisms is grounded in a subset of our numerical results, discussed later, in which secondary wave packets appear to be generated by nonbreaking primary waves.

Secondary waves are identified in the simulation results, to be presented in Sec. IV, as wave packets existing at $O(|A|^2)$. To distinguish waves at this order from those at $O(|A|)$, two simulations are run, one with peak amplitude A_0 and the other by setting $A_0 \to -A_0$ [53,54]. Pairs of results are combined in postprocessing using

$$u^{(1)} = \tfrac{1}{2}(u_+ - u_-), \tag{15}$$

$$u^{(2)} = \tfrac{1}{2}(u_+ + u_-), \tag{16}$$

in which the superscript denotes the order (with respect to $|A|$) of the postprocessed field, and the subscript $+$ or $-$ signs denote whether the associated wave field had positive or negative amplitude.

Upward- and downward-propagating secondary wave packets appear to be generated by distinct mechanisms, described here.

1. Triadic resonant instability

It will be shown that upward-propagating secondary wave packets, generated by the most strongly nonhydrostatic simulated primary waves ($|m_0/k_0| \lesssim 0.7$), result from triadic resonant instability (TRI) between the transmitted and reflected waves. Similarly, it will be shown that downward-propagating secondary wave packets, generated by moderately nonhydrostatic primary waves ($|m_0/k_0| \gtrsim 0.7$) prior to significant wave transmission, do not result from TRI between the incident and reflected waves.

Triadic resonant instability, also known as parametric subharmonic instability, occurs when waves with wave-number vectors $\mathbf{k}_1$ and $\mathbf{k}_2$ and corresponding frequencies $\omega_1 = \omega(\mathbf{k}_1)$ and $\omega_2 = \omega(\mathbf{k}_2)$ interact to produce a third wave with wave-number vector $\mathbf{k}_3$ and frequency $\omega_3 = \omega(\mathbf{k}_3)$ [12,55–57]. In our simulation results, we will identify the wave-number vectors corresponding to transmitted (or incident) and reflected waves as $\mathbf{k}_{\{t,i\}} = \mathbf{k}_1$ and $\mathbf{k}_r = \mathbf{k}_2$, respectively, with corresponding frequencies $\omega_{\{t,i\}}$ and ω_r. The triad interaction equations,

$$\pm\mathbf{k}_{\{t,i\}} \pm \mathbf{k}_r = \pm\mathbf{k}_s, \tag{17}$$

$$\pm\omega_{\{t,i\}} \pm \omega_r = \pm\omega_s, \tag{18}$$

predict wave-number vector and frequency candidates for the secondary waves, $\mathbf{k}_s$ and ω_s. These quantities will be compared to the wave-number vector and frequency of secondary waves, $\mathbf{k}_s^{(2)}$ and $\omega_s^{(2)}$, diagnosed from the results of our numerical simulations.

To diagnose whether TRI is active, the wave-number vectors corresponding to the transmitted (or incident) and reflected wave packets are identified as the Fourier modes corresponding to peaks in the power spectrum of the linear wave field, $|\hat{u}^{(1)}|$, such that

$$\mathbf{k}_{\{t,i\}} = \mathrm{argmax}\{|\hat{u}^{(1)}| : m_{\{t,i\}} < 0\}, \tag{19}$$

$$\mathbf{k}_r = \mathrm{argmax}\{|\hat{u}^{(1)}| : m_r > 0\}. \tag{20}$$

Similarly, the wave-number vector corresponding to secondary waves is identified as the Fourier modes corresponding to a peak in the power spectrum of the quadratically nonlinear wave field: $\mathbf{k}_s^{(2)} = \mathrm{argmax}\{|\hat{u}^{(2)}|\}$.

Because the incident, transmitted, reflected, and secondary waves exist as packets with broad spectra, one does not anticipate that $\mathbf{k}_s = \mathbf{k}_s^{(2)}$ and $\omega_s = \omega_s^{(2)}$ exactly, if indeed TRI is active. For this reason, TRI will be declared as the cause of secondary wave packet generation provided the

predicted $\mathbf{k}_s$ lies within a 50% contour of the spectral peak value $|\hat{u}^{(2)}(\mathbf{k}_s^{(2)})|$, and if ω_s is within 50% of $\omega_s^{(2)}$.

2. Self-reflection

Downward-propagating secondary wave packets appear to be generated prior to reflection by moderately nonhydrostatic primary wave packets ($|m_0/k_0| \gtrsim 0.7$). As a preliminary attempt to explain the unanticipated emergence of these secondary wave packets, we invoke, somewhat heuristically, weakly nonlinear theory to propose a generation mechanism based on self-induced wave reflection.

Linear theory predicts that waves can reflect in a stationary fluid in which the buoyancy frequency decreases with height. Moderately large-amplitude wave packets propagating in an otherwise uniformly stratified ambient locally change the stratification within the volume occupied by the wave packet. The resulting squared total buoyancy frequency, $N_T^2(\mathbf{x}, t)$, is given by (13). Here we derive, for a stationary fluid, the critical amplitude for a wave to reflect partially due to an assumed self-induced local buoyancy decrease, a mechanism we call "self-reflection."

To account for finite amplitude effects, we suppose that a moderately large-amplitude wave packet will induce self-reflection at the height at which its frequency is equal to N_T. We assume the wave-packet frequency is set by the weakly nonlinear dispersion relation, $\omega = \omega_0 + \omega_2 |A|^2$, where ω_2 is a constant to be determined. The term $\omega_2 |A|^2$ accounts for local Doppler-shifting of the waves due to the wave-induced mean flow. Setting $N_T^2 = \omega^2$ and retaining terms of up to $O(|A|^2)$, the weakly nonlinear condition for self-reflection is

$$N_0^2 - N_0^2 \frac{\partial \xi}{\partial z} = \omega_0^2 + 2\omega_0 \omega_2 |A|^2. \tag{21}$$

Self-reflection is anticipated at the height where the left-hand side of (21) is smallest, hence where $\partial \xi / \partial z$ is largest. The coefficient ω_2 is found by analogy with one- and two-dimensional wave packets [17,20,24,38]: Using (10) and setting $\omega_2 |A|^2 = k_0 u_{\mathrm{BF}}(0, 0, z, t = 0)$ in the weakly nonlinear dispersion relation, we find that $\omega_2 = \frac{1}{2} N_0 k_0 \|\mathbf{k}_0\|/(R_y + 1)$. We remark that the value of ω_2 here differs from that for one-dimensional wave packets only by the multiplicative factor $1/(R_y + 1)$.

Substituting ω_2 into (21) and numerically maximizing $\partial \xi / \partial z$, in which $\xi = A_0 \mathcal{A} \cos(k_0 x + m_0 z)$, yields the critical amplitude for secondary wave generation:

$$A_{\mathrm{SW}} = \frac{R_y + 1}{2k_0^2 |\mathcal{A}_*|^2} \left[-M_* + \sqrt{M_*^2 + \frac{4|\mathcal{A}_*|^2}{R_y + 1} \frac{k_0^2 m_0^2}{\|\mathbf{k}_0\|^2}} \right], \tag{22}$$

where $M_*(x_*, z_*) \equiv \max_{x,z}\{\frac{\partial}{\partial z} \mathcal{A} \cos(k_0 x + m_0 z)\}$ with maximizer (x_*, z_*), and $\mathcal{A}_* = \mathcal{A}(x_*, 0, z_*, t = 0)$ in which $\mathcal{A}$ is the amplitude envelope [for example, given for a Gaussian wave packet in (8)]. The critical amplitude A_{SW} was computed numerically with $R_y = 1$, with the result plotted as the dashed blue curve in Fig. 1.

D. Transmission coefficient

Pseudomomentum is one among a family of so-called "wave activity" quantities that is conserved in a nonuniform background flow [26,58–61]. The expression for pseudomomentum density $\mathcal{P}(\mathbf{x}, t)$ corresponding to moderately large-amplitude waves in the xz-plane was derived using Hamiltonian fluid mechanics by [62]. Extending the Hamiltonian approach to three-dimensional small-amplitude disturbances in a Boussinesq fluid, the corresponding expression for the pseudomomentum density [Ref. [63], integrand of Eq. (3.24)] was found to be

$$\mathcal{P}(\mathbf{x}, t) = -\rho_0 \left[\frac{1}{2} \frac{d^2 \bar{u}}{dz^2} \xi^2 + \zeta_y \xi \right], \tag{23}$$

in which $\zeta_y = (\mathbf{\nabla} \times \mathbf{u}) \cdot \hat{\mathbf{e}}_y = \partial u/\partial z - \partial w/\partial x$ is the spanwise component of vorticity. In the limit as $\bar{u} \to 0$, and equivalently in a uniform shear flow, in which $d\bar{u}/dz = s$ is constant, Eq. (23) recovers the expression for pseudomomentum density of small-amplitude monochromatic internal waves confined to propagate in the xz-plane [12], from which the corresponding pseudomomentum is found by averaging over a horizontal wavelength.

Transmission is characterized by the horizontally integrated pseudomomentum density associated with upgoing waves vertically integrated above the reflection level predicted by linear theory. The components of a wave field corresponding to upward- and downward-propagating waves are distinguished using the Hilbert filter [64–66]. Denoting by $H^\uparrow$ ($H^\downarrow$) the Hilbert-filtering operator that extracts upward- (downward-) propagating wave components, we define the pseudomomentum density field associated with upward-propagating waves by

$$\mathcal{P}^\uparrow(\mathbf{x}, t) \equiv -\rho_0 \left[\frac{1}{2} \frac{d^2\bar{u}}{dz^2} (H^\uparrow \xi)^2 + (H^\uparrow \zeta_y)(H^\uparrow \xi) \right]. \tag{24}$$

Explicitly, we define the transmission coefficient by

$$T_\mathcal{P}(t) \equiv \frac{1}{\mathscr{P}_0} \int_{z_r}^{z_{\max}} \langle \mathcal{P}^\uparrow(\mathbf{x}, t) \rangle dz, \tag{25}$$

where $\mathscr{P}_0$ is the (constant) total pseudomomentum, defined by the integral of (23) over the whole spatial domain, and the angle brackets denote integration over the horizontal domain. Because pseudomomentum is conserved, the normalization factor $\mathscr{P}_0$ can in principle be defined at any time t. For numerical convenience, the reasons for which will be discussed below, we set the value of $\mathscr{P}_0$ at $t = 0$ as the total pseudomomentum.

III. NUMERICS

The numerical code was adapted from the one used by [19] to include the effects of Doppler-shifting of the waves by the background flow. Corresponding wave transmission diagnostic abilities were introduced. We also implemented an improved method of damping high wave-number growth arising from the products of perturbation fields.

A. Evolution equations

The fully nonlinear numerical code solved the flux form of the incompressible Boussinesq Euler equations for the horizontal components of velocity (u, v) and perturbation density (recast in terms of vertical displacement ξ), given dimensionally by

$$\frac{\partial u}{\partial t} = -\frac{\partial (p/\rho_0)}{\partial x} - \mathbf{\nabla} \cdot (u\mathbf{u}) - \bar{u}\frac{\partial u}{\partial x} - w\frac{d\bar{u}}{dz}, \tag{26}$$

$$\frac{\partial v}{\partial t} = -\frac{\partial (p/\rho_0)}{\partial y} - \mathbf{\nabla} \cdot (v\mathbf{u}) - \bar{u}\frac{\partial v}{\partial x}, \tag{27}$$

$$\frac{\partial \xi}{\partial t} = w - \mathbf{\nabla} \cdot (\xi\mathbf{u}) - \bar{u}\frac{\partial \xi}{\partial x}, \tag{28}$$

where $\mathbf{u} = (u, v, w)$ is the wave velocity vector. Vertical displacement ξ is related to the perturbation density ρ by $\xi = -\rho/(d\bar{\rho}/dz)$. The dynamic pressure p and vertical velocity fields were found using the diagnostic equations

$$\frac{1}{\rho_0}\nabla^2 p = -\left[\frac{\partial^2(u^2)}{\partial x^2} + \frac{\partial^2(v^2)}{\partial y^2} + \frac{\partial^2(w^2)}{\partial z^2} \right] - 2\left[\frac{\partial^2(uv)}{\partial x \partial y} + \frac{\partial^2(uw)}{\partial x \partial z} + \frac{\partial^2(vw)}{\partial y \partial z} \right]$$
$$- 2\frac{d\bar{u}}{dz}\frac{\partial w}{\partial x} - N_0^2 \frac{\partial \xi}{\partial z}, \tag{29}$$

TABLE I. Initial conditions, domain size and resolution, and predicted reflection height and time for the simulations discussed in the text. Columns are simulation ID, initial peak vertical displacement amplitude nondimensionalized by the streamwise wave number k_0, and as a fraction of the predicted reflection level penetration and secondary wave generation amplitude [A_{RP} and A_{SW}, given by (11) and (22), respectively], shear strength parameter $|s|/N_0$, initial absolute relative vertical wave number $|m_0/k_0|$ and corresponding $\Theta_0 = \tan^{-1}|m_0/k_0|$, domain size $L_x k_0 \times L_y k_0 \times L_z k_0$ and resolution $n_x \times n_y \times n_z$, height of the reflection level predicted by linear theory above the wave-packet initial position, $(z_r - z_0)k_0$, and reflection time $t_r N_0$ predicted by linear theory.

ID	$A_0 k_0$	$\dfrac{A_0}{A_{RP}}$	$\dfrac{A_0}{A_{SW}}$	$\dfrac{|s|}{N_0}$	$\left|\dfrac{m_0}{k_0}\right|$	Θ_0	$L_x k_0 \times L_y k_0 \times L_z k_0$	$n_x \times n_y \times n_z$	$(z_r - z_0)k_0$	$t_r N_0$
S1	0.01	0.03		0.002	0.4	22°	$201.1 \times 200 \times 253.1$	$512 \times 256 \times 512$	50.76	248
S2	0.28	0.95		0.002	0.4	22°	$402.1 \times 200 \times 502.7$	$1024 \times 256 \times 1024$	50.76	248
S3	0.40	1.02	1.07	0.004	0.7	35°	$402.1 \times 200 \times 287.2$	$1024 \times 256 \times 1024$	60.19	214
S4	0.45	1.01	1.08	0.006	1.0	45°	$402.1 \times 200 \times 201.1$	$1024 \times 256 \times 1024$	63.82	208
S5	0.50	1.07	1.21	0.008	1.4	54°	$402.1 \times 200 \times 287.2$	$1024 \times 256 \times 2048$	67.35	227

$$\frac{\partial w}{\partial z} = -\frac{\partial u}{\partial x} - \frac{\partial v}{\partial y}. \tag{30}$$

The spatial structures of Eqs. (26)–(30) were represented by their Fourier spectra [67].

The background flow profile $\bar{u}(z)$ was chosen to be zero from $z_{\min}$ up to just below a "shear onset" height z_s. Centered at z_s was a region in which the background flow transitioned smoothly over a distance L_s to a linearly decreasing shear flow. Explicitly,

$$\bar{u}(z) \equiv \frac{sL_s}{2}\left[\ln\left(1 + e^{-2(z-z_s)/L_s}\right) + 2\frac{z - z_s}{L_s}\right]. \tag{31}$$

In all simulations, the values $L_s = 10 k_0^{-1}$ and $z_s = -20 k_0^{-1}$ were fixed, and shear strength and direction were set by $s < 0$. Values of $|s|$ for a subset of simulations are summarized in Table I. Sample profiles of background flow and its corresponding shear are plotted for a range of shear strength parameters in Fig. 2.

The simulations were initialized using a trivariate Gaussian wave packet, whose vertical displacement field was prescribed by $\xi(\mathbf{x}, 0) = A(\mathbf{x}, 0)\cos[k_0 x + m_0(z - z_0)]$, in which A is given by (8). The wave packet was centered vertically initially at $z_0 = -35 k_0^{-1}$. This was offset below the
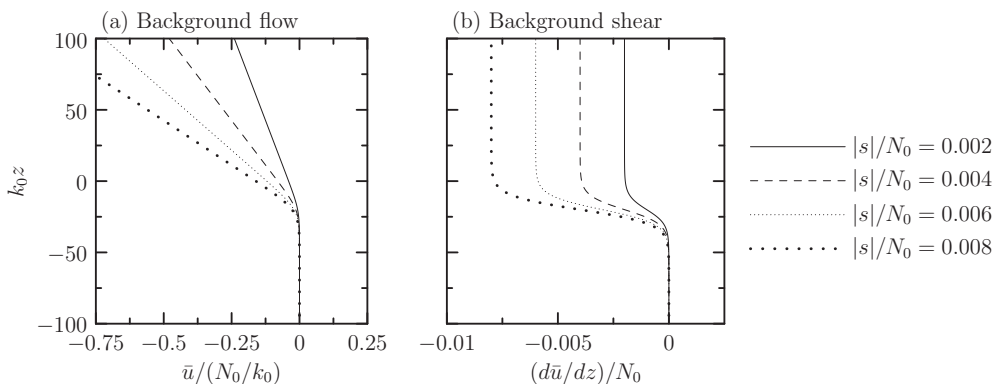

FIG. 2. Profiles of (a) background flow $\bar{u}(z)$, given by (31), with $L_s = 10 k_0^{-1}$ and $z_s = -20 k_0^{-1}$, and (b) the corresponding background shear, $d\bar{u}/dz$.

origin so that at $t = 0$ the background flow was zero over the wave-packet extent, thereby enabling us straightforwardly to initialize the simulations using existing equations for the wave packet and its Bretherton flow derived for an otherwise stationary fluid. The initial horizontal velocity fields (u, v) were set using the polarization relations of Boussinesq internal waves. Superimposed onto u, v, and ξ were their respective envelope-scale corrections, accounting for the finite extent of the wave packet, following the initialization procedure of [19]. The Bretherton flow was superimposed on the horizontal velocity fields using (6) [16,18,36,68].

Space and time scales were set by $k_0 = 1$ and $N_0 = 1$ (arbitrary inverse length and time units, respectively). The spatial domain was triply periodic and of size $L_x \times L_y \times L_z$. The streamwise and vertical dimensions were set using $L_x = 2\pi n_{w,x}/k_0$ and $L_z = 2\pi n_{w,z}/|m_0|$, where $n_{w,x}$ and $n_{w,z}$ were the number of horizontal and vertical wavelengths, respectively, in the domain initially. Typically, $n_{w,x} = 32$ and 64 for small- and moderately large-amplitude simulations, respectively, and $n_{w,z} = 16$, 32, and 64 as relative vertical wave numbers increased from strongly to moderately nonhydrostatic. The spanwise domain size L_y was specified directly, because it was assumed that the domain was oriented such that there was no wave propagation in the spanwise direction (hence the spanwise wave number was $\ell_0 \equiv 0$). The domain size was large enough that neither the waves nor their Bretherton flow would interact with the domain boundaries within the timescales for wave-packet reflection and transmission. Spatial resolution was set by specifying 16 and 32 evenly spaced nodes per wavelength in the streamwise and vertical directions, respectively, following [19]. The domain size and resolution for a subset of simulations is provided in Table I.

Time integration was performed using a low storage third-order accurate Williamson-Runge-Kutta scheme [69,70]. For each simulation, the time step was set to $\Delta t = 0.05 N_0^{-1}$. Simulations performed with a time step of half this size resulted in no significant qualitative or quantitative changes to our solutions.

All simulations were performed in parallel (using 16, 32, or 64 cores) on the Graham, Cedar, and Narval clusters operated by the Digital Research Alliance of Canada [71].

B. Damping of high wave-number growth

Computing quadratic products of perturbation fields results in an unphysical accumulation of power at high wave numbers in the Fourier spectra of the transformed products. To remove power from such high wave numbers, after computing the right-hand sides of Eqs. (26)–(28) the code applied a filter that exponentially damped wave numbers higher than a specified cutoff wave number, κ_{cut} [72,73]. Explicitly, the filter is defined in one dimension by

$$\chi(\kappa) = \begin{cases} 1, & |\kappa| < \kappa_{cut}, \\ \exp\left[-\alpha\left(\frac{|\kappa| - \kappa_{cut}}{\kappa_{nyq} - \kappa_{cut}}\right)^\beta\right], & |\kappa| \geqslant \kappa_{cut}, \end{cases} \tag{32}$$

where α is the filter strength, β is the filter order, and κ_{nyq} and κ_{cut} are the Nyquist and cutoff wave number, respectively. For all simulations, the filter parameters were fixed at the default values of $\alpha = 20$, $\beta = 2$, and $\kappa_{cut} = 0.6\kappa_{nyq}$ described by [73]. Although (32) is defined for streamwise wave numbers κ, in practice (32) was applied in the κ, λ, and μ directions.

C. Transmission diagnostics

The code Hilbert-filtered the spectral representations of ξ and ζ_y to extract the upward-propagating components of these fields [65]. The resulting (real) fields were used in (24), which was integrated spatially and normalized by the initial (total) pseudomomentum $\mathscr{P}_0$ according to (25).

Although in theory $\mathscr{P}_0$ is conserved for small-amplitude disturbances, in practice the accumulation of small numerical errors causes the total pseudomomentum to vary from its initial value as a simulation evolves. To quantify this discrepancy, we define the relative pseudomomentum error at

any time t by

$$\mathscr{P}_{\mathrm{err}}(t) \equiv \left| 1 - \frac{\mathscr{P}_{\mathrm{tot}}(t)}{\mathscr{P}_0} \right| \times 100\%, \tag{33}$$

where $\mathscr{P}_{\mathrm{tot}}(t) = \int_{\mathcal{D}} \mathcal{P}(\mathbf{x}, t) dx\, dy\, dz$ is the pseudomomentum density integrated over the spatial domain $\mathcal{D}$. We somewhat heuristically set a confidence threshold of $\mathscr{P}_{\mathrm{err}} < 1\%$ and assume simulation results are reliable provided the relative pseudomomentum error is within this tolerance. In practice, this tolerance was typically met over times $N_0 t \lesssim 400$, during which quasisteady final transmission was established.

IV. RESULTS

Our intent is to quantify the transmission of localized wave packets above the reflection level predicted by linear theory for the background flow profile prescribed by (31), and to explain the mechanisms driving their linear and nonlinear evolution. Numerical simulations evolved wave packets with initial amplitudes between $A_0 = 0.01 k_0^{-1} \approx 0.0016 \lambda_{x0}$ and $A_0 = 0.55 k_0^{-1} \approx 0.0875 \lambda_{x0}$, and initial relative vertical wave numbers between $m_0 = -0.4 k_0$ and $-1.4 k_0$, thus spanning a range of small- to moderately large-amplitude nonhydrostatic wave packets propagating upward and rightward initially. The choice of shear strength parameter was set somewhat heuristically by the initial relative vertical wave number such that waves were predicted by linear theory to reflect in the range $50 \lesssim (z_r - z_0) k_0 \lesssim 70$. This range was deemed to be far enough above z_0 for the waves to begin evolving nonlinearly prior to reflection, and far enough below the top boundary for reflected and transmitted waves to remain within the domain for the duration of the simulation. Our investigation focused on initially "round" wave packets, for which we fixed $\sigma_x = \sigma_y = \sigma_z = 10 k_0^{-1}$. We performed a total of 38 simulations. The domain and initialization parameters of the subset of simulations explicitly discussed in text are summarized in Table I.

A. Evolution of strongly nonhydrostatic wave packets

We examine first the evolution of a small-amplitude Gaussian wave packet with $m_0 = -0.4 k_0$, and we describe its partial transmission above and reflection below the reflection level predicted by linear theory. We then examine moderately large-amplitude wave packets, with an emphasis on their nonlinear evolution, and the effects of amplitude on transmission.

1. Small-amplitude wave packet: Linear evolution

Snapshots of streamwise velocity $\tilde{u} = u / \max\{u(\mathbf{x}, 0)\}$ through the $y = 0$ plane of a small-amplitude wave packet with $A_0 = 0.01 k_0^{-1}$ and $m_0 = -0.4 k_0$ (simulation S1 in Table I) are shown in Fig. 3. The times shown in each panel are representative of the wave packet at early, prereflection, postreflection, and late times. Profiles of the background flow and its shear used in this simulation are plotted as the solid curves in Fig. 2.

Initially [Fig. 3(a)] the lines of constant phase were oriented at $\Theta_0 \approx 22°$ from the vertical, and the wave packet propagated upward and rightward at this angle in agreement with linear theory. Upward propagation was confirmed by the overlap between the profiles of $\langle \tilde{\mathcal{P}}^{\uparrow} \rangle$ and $\langle \tilde{\mathcal{P}} \rangle$. At $t = 150/N_0$ [Fig. 3(b)], the leading flank of the wave packet had propagated into the background shear flow, and the lines of constant phase were more strongly oriented toward the vertical in response to the increased Doppler-shifted frequency. A relatively small amount of downward-propagating pseudomomentum $\langle \tilde{\mathcal{P}}^{\downarrow} \rangle$ accumulated below z_r, indicating reflection began well before the time $t_r = 248/N_0$ predicted by linear theory. The vertical extent of $\langle \tilde{\mathcal{P}} \rangle$ broadened due to linear dispersion, and its peak value decreased as a consequence of pseudomomentum conservation. At $t = 300/N_0$ [Fig. 3(c)], much of the wave packet had reflected and began propagating downward, indicated by the overlap between the profiles of $\langle \tilde{\mathcal{P}}^{\downarrow} \rangle$ and $\langle \tilde{\mathcal{P}} \rangle$.
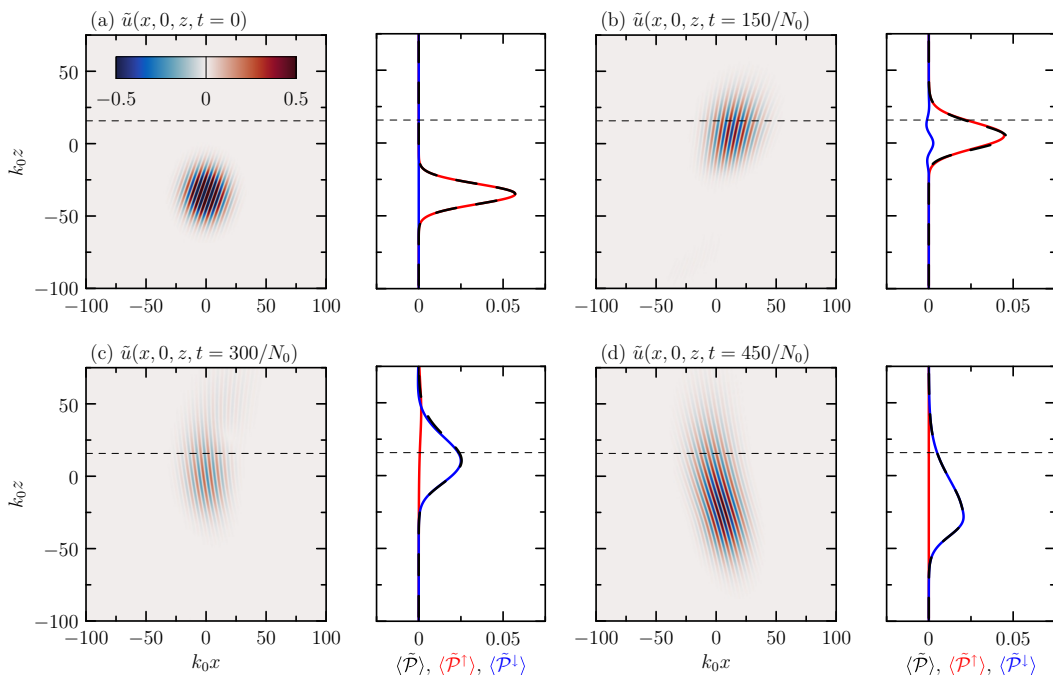
FIG. 3. Cross sections of streamwise velocity $\tilde{u} = u/\max\{u(\mathbf{x}, 0)\}$ through the vertical plane $y = 0$ of a small-amplitude wave packet with $A_0 = 0.01k_0^{-1}$ and $m_0 = -0.4k_0$ at times $t = 0$ (a), $150/N_0$ (b), $300/N_0$ (c), and $450/N_0$ (d). The corresponding right panels show vertical profiles of horizontally integrated pseudomomentum density normalized by $k_0 \mathscr{P}_0$. The red and blue curves are of the upward- and downward-propagating parts, $\langle \tilde{\mathcal{P}}^\uparrow \rangle$ and $\langle \tilde{\mathcal{P}}^\downarrow \rangle = \langle \tilde{\mathcal{P}} \rangle - \langle \tilde{\mathcal{P}}^\uparrow \rangle$, respectively, in which $\langle \tilde{\mathcal{P}} \rangle$ is the total distribution (dashed black curves). Image resolution was doubled in postprocessing, and images were cropped to focus on the region containing the wave packet. The horizontal dashed line in each panel indicates the height of the reflection level, $z_r = 15.76k_0^{-1}$, predicted by linear theory. See movie 1 in the Supplemental Material [74].

A time series of upward-propagating pseudomomentum above z_r for this simulation is shown as the solid black curve in Fig. 4. This time series reveals there was a transient penetration of pseudomomentum above z_r beginning shortly after $t = 100/N_0$, peaking at $t^* = 218/N_0$ before the predicted reflection time of $t_r = 248/N_0$. At late times, $t \gtrsim 350/N_0$, negligible pseudomomentum remained above the reflection level.

2. Moderately large-amplitude wave packet: Transmission, reflection, and secondary wave generation

Moderately large-amplitude wave packets are non-negligibly influenced by nonlinear interactions with their induced mean (Bretherton) flow. Snapshots of the evolution of one such wave packet (S2) with $A_0 = 0.28k_0^{-1}$ and $m_0 = -0.4k_0$ are shown in Fig. 5. This velocity field is decomposed into $O(|A|)$ contributions, $\tilde{u}^{(1)}$, and $O(|A|^2)$ contributions, $\tilde{u}^{(2)}$, using (15) and (16), respectively.

Initially, the velocity fields $\tilde{u}$ and $\tilde{u}^{(1)}$ are nearly identical [Figs. 5(a) and 5(b)], and $\tilde{u}^{(2)} = u_{\text{BF}}$, whose Gaussian structure is shown clearly in Fig. 5(c). Nonlinearity was evident at $t = 150/N_0$, indicated by the anticipated steepening (flattening) of phase lines above (below) the center of the wave packet [Figs. 5(e) and 5(f)], located near $z = 0$. The vertical extent of the Bretherton flow narrowed and its amplitude grew [Fig. 5(g)] as a consequence of modulational instability. At $t = 300/N_0$, the wave packet exhibited three distinct features [Fig. 5(i)]: A transmitted wave packet propagated upward and to the right above z_r; a reflected wave packet propagated downward; and an asymmetric upward-propagating *secondary wave packet* radiated toward the left, with phase lines
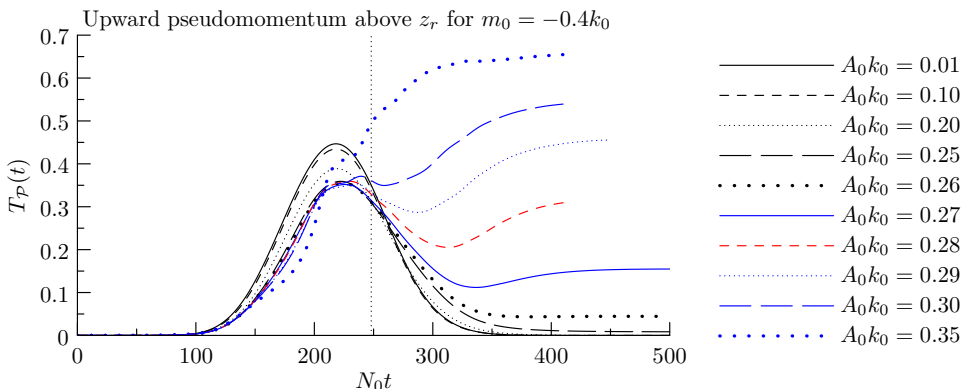
FIG. 4. Time series of upward-propagating pseudomomentum above z_r, where $T_{\mathcal{P}}(t)$ is given by (25), for the subset of simulations performed with $m_0 = -0.4k_0$. The vertical dotted line indicates the time $N_0 t_r = 248$ at which reflection was predicted by linear theory. Data are plotted either to the end time of their respective simulations, or until the first time a relative pseudomomentum error of $\mathscr{P}_{\mathrm{err}} \geqslant 1\%$ was diagnosed, whichever occurred earlier.

approximately perpendicular to those of the reflected wave packet. The secondary waves are shown in Fig. 5(k), superimposed with the mean flow induced by the reflecting wave packet. The profile of $\langle \tilde{\mathcal{P}}^\downarrow \rangle$ corresponding to the latter accounted for most of the total pseudomomentum below z_r. At $t = 450/N_0$, the three wave packets had separated [Fig. 5(m)]. In particular, the transmitted wave packet penetrated well above z_r, being associated with $\langle \tilde{\mathcal{P}}^\uparrow \rangle$ between $25k_0^{-1}$ and $75k_0^{-1}$ [Fig. 5(p)].

That the secondary waves in Fig. 5 existed at $O(|A|^2)$ indicates they were generated nonlinearly. In particular, we find these to have been generated by triadic resonant instability between the transmitted and reflected wave packets. The wave-number vectors and frequencies corresponding to the respective wave packets are included in Table II. The predicted and diagnosed spectral peaks $\mathbf{k}_s$ and $\mathbf{k}_s^{(2)}$, and corresponding frequencies ω_s and $\omega_s^{(2)}$, agreed to within 95%. Crucially, the secondary waves were generated by nonbreaking primary waves, as we confirmed by evaluating the overturning condition (14) through the duration of the simulation: $\min\{N_T^2\} \gtrsim 0.8N_0^2$, in which N_T^2 is given by (13).

A time series of upward-propagating pseudomomentum above z_r for S2 is plotted as the dashed red curve in Fig. 4. The time series shows a peak at $t^* \approx 230/N_0$. Unlike the small-amplitude simulation (S1), transmission in S2 decreased until $t = 313/N_0$, after which transmission increased once more. Transmission started tending toward a fixed value as the bulk of the transmitted wave packet penetrated above z_r.

Vertical time series of $\langle \tilde{\mathcal{P}}^\uparrow \rangle$ and $\langle \tilde{\mathcal{P}}^\downarrow \rangle$ for S2 are shown in Figs. 6(a) and 6(b), respectively. Modulational instability is evident by the increased peak value of $\langle \tilde{\mathcal{P}}^\uparrow \rangle$ and the slightly narrowed vertical extent of the wave packet. From $t \approx 200/N_0$ onward, transmitted waves propagate upward with approximately fixed vertical group speed.

3. Amplitude dependence of transmission

Time series of upward-propagating pseudomomentum above z_r for strongly nonhydrostatic wave packets with $m_0 = -0.4k_0$ and initial amplitudes ranging from small ($A_0 = 0.01k_0^{-1} \approx 0.03A_{\mathrm{RP}}$) to moderately large ($A_0 = 0.35k_0^{-1} \approx 1.19A_{\mathrm{RP}}$) are shown in Fig. 4. As the wave-packet initial amplitude increased, three trends emerged: The onset of upward pseudomomentum penetration above z_r and the time of peak transmission were delayed; for $A_0 \leqslant 0.28k_0^{-1}$, the wave packets exhibited an increasing, then decreasing, transmission above z_r, but for $A_0 > 0.28k_0^{-1}$, transmission increased again; at late times, the transmission remained nonzero for $A_0 \geqslant 0.25k_0^{-1}$.
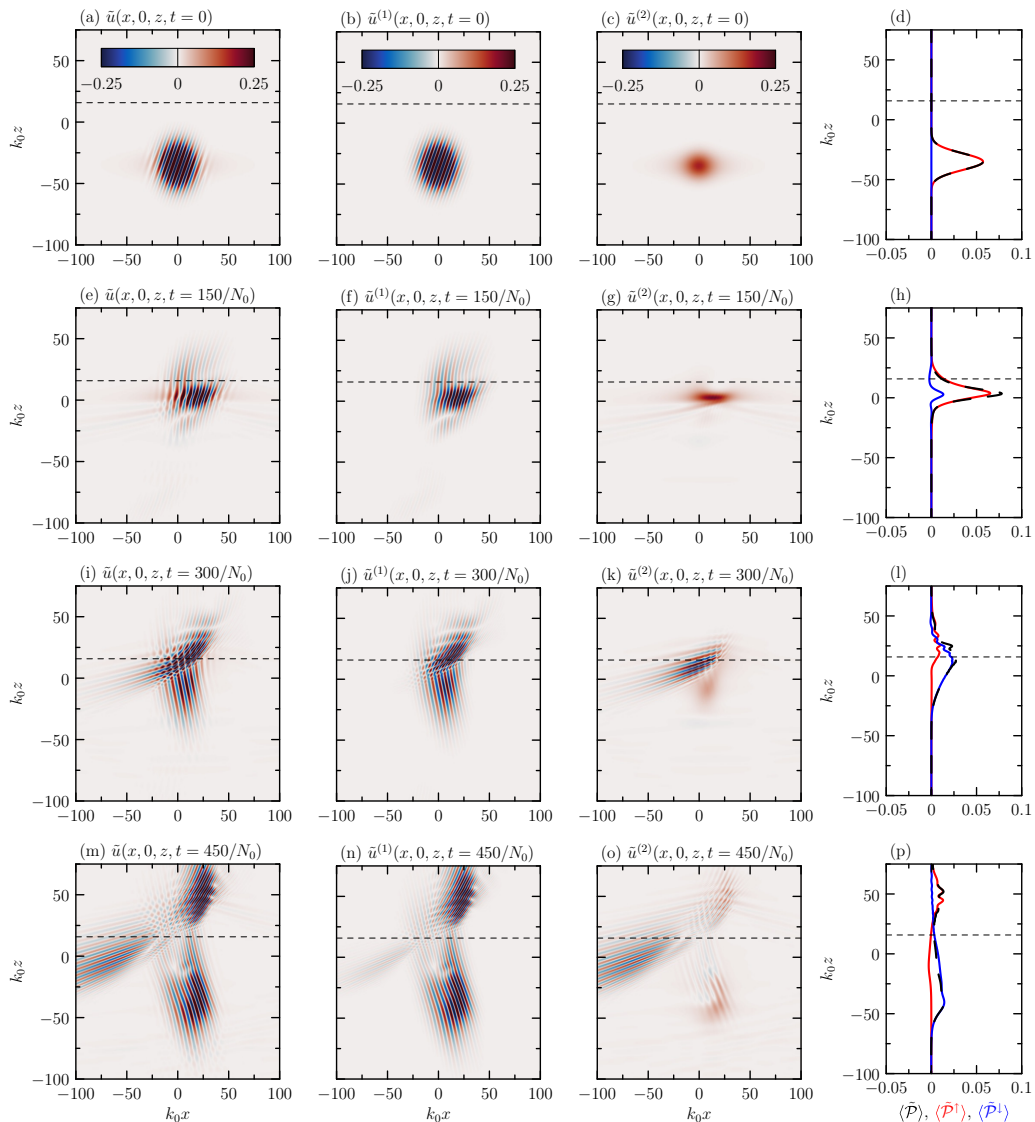
FIG. 5. As in Fig. 3 but for a moderately large amplitude wave packet with $A_0 = 0.28k_0^{-1}$ at times $t = 0$ (a)–(d), $150/N_0$ (e)–(h), $300/N_0$ (i)–(l), and $450/N_0$ (m)–(p). The three leftmost columns are of, respectively, total streamwise velocity $\tilde{u}$, and its constituent $O(|A|)$ and $O(|A|^2)$ parts, denoted by $\tilde{u}^{(1)}$ and $\tilde{u}^{(2)}$, respectively, given by (15) and (16), respectively. The dashed line in each panel indicates the height of the reflection level, $z_r = 15.76k_0^{-1}$, predicted by linear theory. See movie 2 in the Supplemental Material [74].

The delayed onset and peak times of pseudomomentum penetration above z_r were due to modulational instability acting to retard the vertical advance of the incident wave packets. The observed post-first peak decreases of transmission corresponded to downward transport of pseudomomentum by the reflected wave packets, and the subsequent increases resulted from the upward propagation of transmitted primary, and eventually radiated secondary, wave packets. Decreasing peak transmission with initial amplitude up to $A_0 = 0.28k_0^{-1}$ was due to the radiation of progressively larger-amplitude secondary waves below z_r, which retained at least some of their pseudomomentum below z_r until

TABLE II. Data used to diagnose triadic resonant instability (TRI) for a given simulation and time. Center columns: Streamwise and vertical Fourier modes corresponding to the spectral peak of transmitted (or incident) and reflected wave packets [$(k_{\{t,i\}}, m_{\{t,i\}}) = \mathbf{k}_{\{t,i\}}$ and $(k_r, m_r) = \mathbf{k}_r$, respectively], and their corresponding frequencies, $\omega_{\{t,i\}} = \omega(\mathbf{k}_{\{t,i\}})$ and $\omega_r = \omega(\mathbf{k}_r)$, diagnosed from the power spectrum of the linear wave field $u^{(1)}$. Center-right column: Fourier modes corresponding to the spectral peak of secondary wave packets diagnosed from the power spectrum of the quadratically nonlinear wave field $u^{(2)}$ [$(k_s^{(2)}, m_s^{(2)}) = \mathbf{k}_s^{(2)}$], and corresponding frequency, $\omega_s^{(2)} = \omega(\mathbf{k}_s^{(2)})$. The rightmost column indicates whether TRI is suspected as the cause of the secondary waves according to the criteria in Sec. II C 1.

ID	$N_0 t$	Transmitted (or incident)			Reflected			Secondary			TRI
		$k_{\{t,i\}}/k_0$	$m_{\{t,i\}}/k_0$	$\omega_{\{t,i\}}/N_0$	k_r/k_0	m_r/k_0	ω_r/N_0	$|k_s^{(2)}|/k_0$	$m_s^{(2)}/k_0$	$\omega_s^{(2)}/N_0$	
S2	300	1.34	-1.20	0.75	0.95	0.20	0.98	0.36	-1.34	0.26	yes
S3	150	1.05	-0.57	0.88	1.00	0.13	0.99	0.16	0.68[a]	0.22	no
S4	150	1.00	-0.72	0.81	1.03	0.16	0.99	0.27	0.84[a]	0.30	no
S5	200	1.00	-0.77	0.79	1.03	0.39	0.93	0.25	0.83[a]	0.29	no

[a]Secondary waves identified are those propagating downward and rightward, assuming TRI between incident and reflected waves (transmitted waves not yet present).

after primary wave transmission had peaked. The trend reversed for wave packets with initial amplitudes $A_0 \geqslant 0.29 k_0^{-1} \approx 0.99 A_{\mathrm{RP}}$.

B. Evolution of moderately nonhydrostatic wave packets

Here we examine the evolution of moderately large-amplitude wave packets initialized with $m_0 = -0.7k_0$ (S3), $-k_0$ (S4), and $-1.4k_0$ (S5). The simulations were chosen such that their initial amplitudes were greater than both the predicted amplitudes for reflection level penetration, A_{RP}, and secondary wave generation, A_{SW}, given by (11) and (22), respectively.

The streamwise velocity from S3 ($A_0 = 0.4k_0^{-1}$) at $t = 200/N_0$ is shown in Fig. 7(a). Like S2, upward-propagating secondary waves were radiated leftward, likely as a result of triadic resonant instability (TRI) between the transmitted and reflected wave packets. Unlike S2, *downward-* and *rightward-propagating* secondary waves were also radiated by the incident wave packet, existing at $t = 200/N_0$ as a distinct secondary wave packet with broad streamwise extent, spatially disjoint from the other wave packets. Simulations S4 [$A_0 = 0.45k_0^{-1}$; Fig. 7(b)] and S5 [$A_0 = 0.5k_0^{-1}$; Fig. 7(c)] similarly evolved to exhibit reflection and partial transmission, but with secondary waves radiated preferentially by the (nonbreaking) incident wave packet. TRI could not be identified within
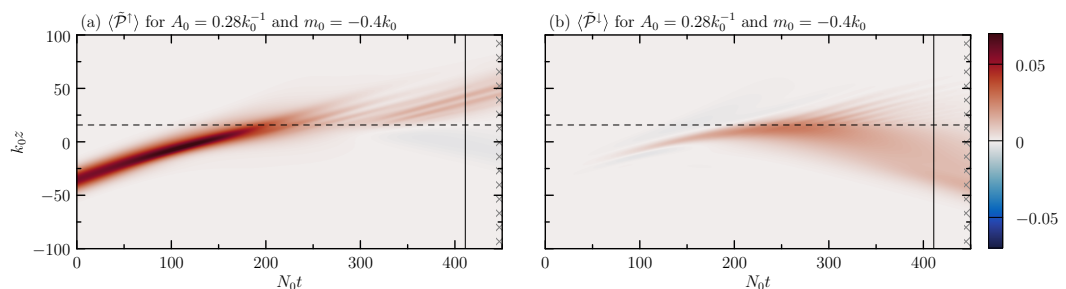

FIG. 6. Vertical time series of (a) $\langle \tilde{\mathcal{P}}^\uparrow \rangle$ and (b) $\langle \tilde{\mathcal{P}}^\downarrow \rangle$ for simulation S2. Image resolution was doubled in postprocessing. The horizontal dashed line indicates the height of the reflection level $z_r = 15.76k_0^{-1}$ predicted by linear theory, the vertical line indicates the first time, $t = 411/N_0$, at which $\mathcal{P}_{\mathrm{err}} \geqslant 1\%$, and crosshatching indicates the time $t \geqslant 444/N_0$ for which $\mathcal{P}_{\mathrm{err}} \geqslant 5\%$.
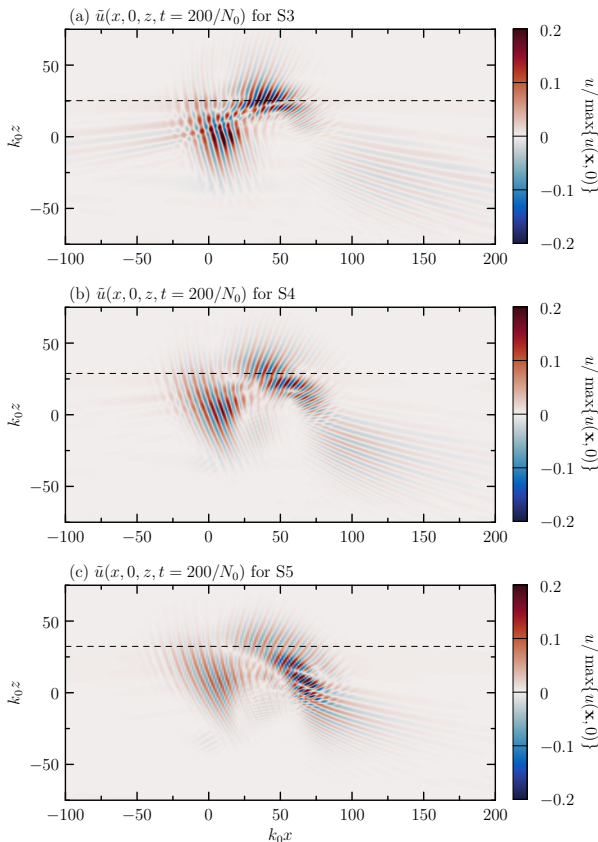
FIG. 7. As in the leftmost columns of Figs. 3 and 5 but at $t = 200/N_0$ for simulation (a) S3, in which $A_0 = 0.4k_0^{-1}$ and $m_0 = -0.7k_0$; (b) S4, in which $A_0 = 0.45k_0^{-1}$ and $m_0 = -k_0$; and (c) S5, in which $A_0 = 0.5k_0^{-1}$ and $m_0 = -1.4k_0$. The horizontal dashed lines indicate the respective heights of the reflection level predicted by linear theory, $z_r = 25.19k_0^{-1}$ (a), $28.82k_0^{-1}$ (b), and $32.35k_0^{-1}$ (c). For the evolution of S5, see movie 3 in the Supplemental Material [74].

the 50% threshold from the power spectra of the linear and quadratically nonlinear wave fields from S3–5 (cf. Table II). The diminishing prevalence of upward-propagating secondary waves in S2–5 may be due in part to the increasing shear strength in these simulations. Increasing shear strength was found to suppress TRI in simulations of one-dimensional wave packets incident upon a retrograde jet [75] by shortening the time interval during which the incident and reflected wave spectra evolved within the resonant regime. Finally, we remark that secondary wave fronts in the horizontal plane $z = z_0 - c_{gz}t$ (not shown) resemble qualitatively the radially propagating waves generated by an oscillating sphere [76,77]. However, this linear generation mechanism accounts for neither the amplitude-squared nature of the secondary waves, nor their preferential direction of radiation, suggesting a similar mechanism is not active in S3–5. Ruling out these mechanisms, we suggest that downward- and rightward propagating secondary wave packets may have been generated by self-reflection.

Although S3 and S4–5 were, respectively, marginally stable and modulationally stable initially, Doppler-shifting of the frequency by $\bar{u}$ eventually drove the wave packets to become modulationally unstable after $t \approx 75/N_0$ [for S3–4; Figs. 8(a) and 8(c)]. The modulational stability of S5 was sufficiently strong initially that the destabilizing effect of $\bar{u}$ was less pronounced, and resulted in a succession of narrowing and peaking events below z_r during $125 \lesssim N_0 t \lesssim 200$ in Fig. 8(e).
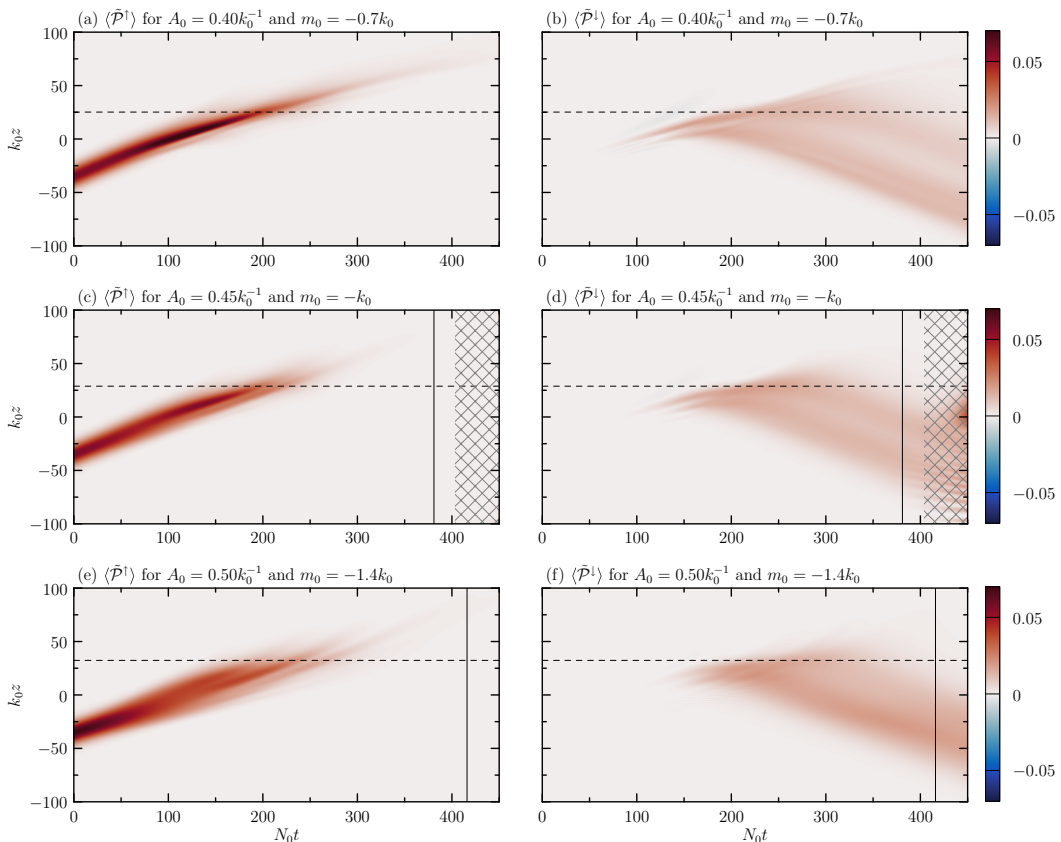
FIG. 8. As in Fig. 6 but for simulations S3 (a), (b); S4 (c), (d); and S5 (e), (f). The vertical lines in (c), (d) and (e), (f) indicate the first times, $t = 381/N_0$ and $416/N_0$, respectively, that $\mathscr{P}_{\text{err}} \geqslant 1\%$, and crosshatching in (c), (d) indicates the time $t \geqslant 404/N_0$ for which $\mathscr{P}_{\text{err}} \geqslant 5\%$.

Vertical time series of $\langle \tilde{\mathcal{P}}^{\downarrow} \rangle$ in Figs. 8(b), 8(d), and 8(f) are qualitatively similar among S3–5 and S2. In particular, there existed downward-propagating pseudomomentum well below z_r prior to t_r, due in part to the concurrent radiation of downward-propagating secondary waves generated by the respective incident wave packets.

C. Transmission analysis

The first peak transmission coefficient $T^*_{\mathcal{P}} = T_{\mathcal{P}}(t^*)$, in which t^* is the time of first peak transmission, is shown as the black data in Fig. 9(a) for a range of initial amplitudes and relative vertical wave numbers. As amplitude increased, peak transmission generally decreased, except for the wave packets with $m_0 = -0.4k_0$ (diamonds). Black and blue diamonds, respectively, show $T^*_{\mathcal{P}}$ and $T_{\mathcal{P}}(t = 400/N_0)$, reproduced from the time series in Fig. 4. Peak transmission of wave packets with $m_0 = -k_0$ and $-1.4k_0$ tended to decrease with amplitude. The smallest first peak transmission coefficient for these wave packets was $T^*_{\mathcal{P}} = 0.24$ and 0.16, respectively, in each case corresponding to wave packets with the largest initial amplitude $A_0 = 0.55k_0^{-1}$. This resulted from the envelope-broadening and attenuating effects of modulational stability, and the downward transport of otherwise available pseudomomentum by secondary wave packets. For wave packets with $m_0 = -0.7k_0$, the smallest $T^*_{\mathcal{P}} = 0.32$ was diagnosed for $A_0 = 0.3k_0^{-1} \approx 0.77A_{\text{RP}} \approx 0.80A_{\text{SW}}$. Finite transmission above z_r at late times, $T_{\mathcal{P}}(t = 400/N_0)$, is indicated by the respective blue
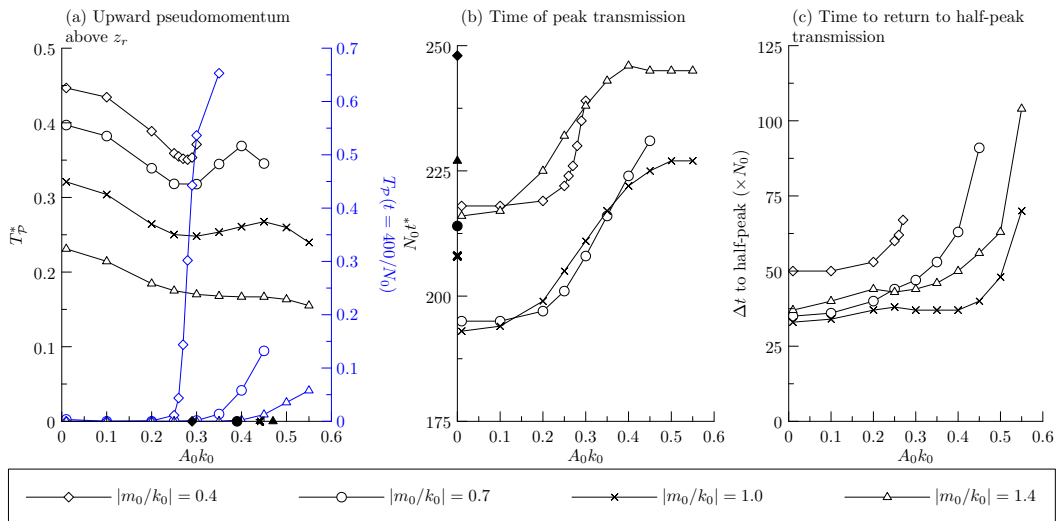
FIG. 9. Transmission diagnostics: (a) $T_\mathcal{P}^*$ (black) and $T_\mathcal{P}(t = 400/N_0)$ (blue), in which the bold symbols on the horizontal axis indicate A_{RP}; (b) t^*, the time at which first peak transmission was diagnosed, in which the bold symbols on the vertical axis indicate $N_0 t_r$; (c) Δt, the time required for transmission to return to half its maximum value shown in (a). Data at $t = 400/N_0$ for $m_0 = -k_0$ were excluded from (a) because $\mathscr{P}_{\mathrm{err}} \geqslant 1\%$ before $t = 400/N_0$ in the moderately large amplitude cases. Select black data points in (a) and (b) had their corresponding data point in (c) excluded because either $\mathscr{P}_{\mathrm{err}} \geqslant 1\%$ before Δt could be attained, or transmission did not decay to half its peak value during the simulation.

symbols. This is less pronounced for wave packets with $m_0 = -0.7k_0$ and $-1.4k_0$ than for those with $-0.4k_0$, although in all cases finite transmission occurred with initial amplitudes less than A_{RP}.

The time t^* at which first peak transmission occurred is shown in Fig. 9(b). All but the largest-amplitude wave packet with $m_0 = -0.4k_0$ (which lacked a clear first transmission peak) exhibited increasing values of t^* due to modulational instability acting to retard the vertical advance of the wave packets. Increasing initial amplitude shortened the timescales for growth of this instability, and promoted the generation of upward-propagating secondary waves. Modulational instability was similarly responsible for increasing values of t^* in simulations with $m_0 = -0.7k_0$. The trend of increasing values of t^* for wave packets with $m_0 = -k_0$ and $-1.4k_0$ was less pronounced, tending toward fixed values of $t^* = 227/N_0$ and $245/N_0$, respectively.

Because $T_\mathcal{P}$ was a transient quantity, we diagnosed the time interval Δt required for transmission above z_r to decay to half the value of $T_\mathcal{P}^*$ [Fig. 9(c)]. For wave packets with $m_0 = -0.4k_0$ and $0.01 \leqslant A_0 k_0 \leqslant 0.27$, Δt increased with increasing initial amplitude. Transmission above z_r did not decay to half the corresponding values of $T_\mathcal{P}^*$ for $A_0 \geqslant 0.28 k_0^{-1}$ due to pronounced penetration of primary waves.

V. DISCUSSION AND CONCLUSIONS

Internal gravity wave packets evolving in nonuniform retrograde background shear flow transiently transmit across a reflection level. Depending on the wave number and amplitude, the characteristics of transmission can vary significantly.

We predicted critical amplitudes for "reflection level penetration," above which there is finite transmission above the reflection level at late times, and "self-reflection," a mechanism that predicts when significant generation of secondary wave packets by nonbreaking primary waves occurs.

We investigated these predictions by performing fully nonlinear simulations of nonhydrostatic three-dimensional wave packets incident upon a retrograde shear flow. Nonlinear interactions between moderately large amplitude strongly (moderately) nonhydrostatic wave packets and their Bretherton flow led to modulational instability (stability). The corresponding nonlinearly generated upward- (downward-) propagating secondary wave packets acted ultimately to enhance (hinder) transmission above the predicted reflection level.

The reflection level penetration condition (11) was generally effective to predict whether a wave packet would exhibit finite transmission above the reflection level z_r at late times. For example, strongly nonhydrostatic wave packets with $m_0 = -0.4k_0$ and initial amplitudes as small as $A_0 = 0.25k_0^{-1} \approx 0.85A_{\mathrm{RP}}$ transmitted partially above z_r with $T_{\mathcal{P}}(t = 400/N_0) \approx 0.01$. Similarly, wave packets with $m_0 = -0.7k_0$ and $-1.4k_0$ exhibited finite transmission $T_{\mathcal{P}}(t = 400/N_0) \gtrsim 0.01$ with $A_0 \geqslant 0.35k_0^{-1} \gtrsim 0.9A_{\mathrm{RP}}$ and $A_0 \geqslant 0.45k_0^{-1} \gtrsim 0.97A_{\mathrm{RP}}$, respectively. The existence of transmitted pseudomomentum above z_r at late times is analogous to the "steady-state" transmission identified by Sutherland [38]. In contrast with the ray-theory results of Robinson [37], but in agreement with the fully nonlinear simulation results of Ref. [38], three-dimensional wave packets that exhibited finite transmission above z_r at late times did not encounter a vertically displaced reflection level higher up.

Triadic resonant instability between transmitted and reflected wave packets was identified as generating upward-propagating secondary waves in the most strongly nonhydrostatic simulations, but not the downward-propagating secondary waves characteristic of moderately nonhydrostatic simulations. The proposed "self-reflection" condition for secondary wave-packet generation by nonbreaking moderately nonhydrostatic primary waves tended to overpredict the critical initial amplitude, A_{SW}, for the onset of this mechanism. To assess qualitatively the degree to which $\bar{u}(z)$ may have contributed to this result, a subset of our simulations was repeated, but with $\bar{u} \equiv 0$. Compared to simulations with nonuniform background flow, the prediction for secondary wave generation was generally well borne out for nonhydrostatic wave packets with $-0.7k_0$ and $\bar{u} \equiv 0$ (not shown). Secondary wave packets typically became evident on approximately the same timescale as in the simulations with nonuniform background flow. The critical amplitude was underpredicted for wave packets with $m_0 = -k_0$ and $-1.4k_0$ and $\bar{u} \equiv 0$ (not shown). To better assess the robustness of the prediction for secondary wave-packet generation, future work will adopt quantitative diagnostics to analyze secondary wave packets. Using weakly (fully) nonlinear WKBJ (wave-resolving and large-eddy simulation) methods, Muraschko et al. [78] examined the propagation of one-dimensional wave packets in a range of background flow and stratification profiles. Although wave-packet evolution was captured by their weakly and fully nonlinear codes, no secondary waves were identified. This suggests that the qualitative behaviors of our secondary waves (in particular those propagating downward) may represent dynamics unique to fully localized three-dimensional wave packets.

Our theory and simulations provide insight into the mechanisms governing wave-packet evolution in a nonuniform background flow. However, our results are highly idealized, having assumed a uniformly stratified, infinite Boussinesq fluid with a steady, horizontally homogeneous but vertically nonuniform background flow. Ongoing work is extending the study of three-dimensional wave-packet transmission and reflection to a nonuniformly stratified anelastic gas.

[1] D. C. Fritts and M. J. Alexander, Gravity wave dynamics and effects in the middle atmosphere, Rev. Geophys. **41**, 1003 (2003).

[2] B. R. Sutherland, U. Achatz, C.-c. P. Caulfield, and J. M. Klymak, Recent progress in modeling imbalance in the ocean and atmosphere, Phys. Rev. Fluids **4**, 010501 (2019).

[3] D. C. Fritts, S. L. Vadas, K. Wan, and J. A. Werne, Mean and variable forcing of the middle atmosphere by gravity waves, J. Atmos. Sol. Terr. Phys. **68**, 247 (2006).

[4] M. H. Alford, J. A. MacKinnon, H. L. Simmons, and J. D. Nash, Near-inertial internal gravity waves in the ocean, Annu. Rev. Mar. Sci. **8**, 95 (2016).

[5] J. M. Cusack, A. C. Naveira Garabato, D. A. Smeed, and J. B. Girton, Observation of a large lee wave in the Drake Passage, J. Phys. Oceanogr. **47**, 793 (2017).

[6] R. B. Smith, 100 years of progress on mountain meteorology research, in *A Century of Progress in Atmospheric and Related Sciences: Celebrating the American Meteorological Society Centennial*, Meteor. Mon. (American Meteorological Society, Boston, USA, 2018), Chap. 20, Vol. 59, pp. 20.1–20.73.

[7] C. R. Homeyer, J. D. McAuliffe, and K. M. Bedka, On the development of above-anvil cirrus plumes in extratropical convection, J. Atmos. Sci. **74**, 1617 (2017).

[8] M. E. O'Neill, L. Orf, G. M. Heymsfield, and K. Halbert, Hydraulic jump dynamics above supercell thunderstorms, Science **373**, 1248 (2021).

[9] C. J. Wright, Quantifying the global impact of tropical cyclone-assisted gravity waves using HIRDLS, MLS, SABER, and IBTrACS data, Q. J. R. Meteorol. Soc. **145**, 3023 (2019).

[10] B. Kaifler, N. Kaifler, B. Ehard, A. Dörnbrack, M. Rapp, and D. C. Fritts, Influence of source conditions on mountain wave penetration into the stratosphere and mesosphere, Geophys. Res. Lett. **42**, 9488 (2015).

[11] M. Bramberger, A. Dörnbrack, K. Bossert, B. Ehard, D. C. Fritts, B. Kaifler, C. Mallaun, A. Orr, P.-D. Pautet, M. Rapp, M. J. Taylor, S. Vosper, B. P. Williams, and B. Witschas, Does strong tropospheric forcing cause large-amplitude mesospheric gravity waves? A DEEPWAVE case study, J. Geophys. Res. Atmos. **122**, 11422 (2017).

[12] B. R. Sutherland, *Internal Gravity Waves* (Cambridge University Press, Cambridge, UK, 2010), p. 378.

[13] F. P. Bretherton, On the mean motion induced by gravity waves, J. Fluid Mech. **36**, 785 (1969).

[14] O. Bühler, *Waves and Mean Flows* (Cambridge University Press, Cambridge, UK, 2009), p. 341.

[15] T. G. Shepherd, Symmetries, conservation laws, and Hamiltonian structure in geophysical fluid dynamics, Adv. Geophys. **32**, 287 (1990).

[16] T. S. van den Bremer and B. R. Sutherland, The mean flow and long waves induced by two-dimensional internal gravity wavepackets, Phys. Fluids **26**, 106601 (2014).

[17] A. D. Gervais, G. E. Swaters, T. S. van den Bremer, and B. R. Sutherland, Evolution and stability of two-dimensional anelastic internal gravity wave packets, J. Atmos. Sci. **75**, 3703 (2018).

[18] T. S. van den Bremer and B. R. Sutherland, The wave-induced flow of wide three-dimensional internal gravity wavepackets, J. Fluid Mech. **834**, 385 (2018).

[19] A. D. Gervais, Q. Ede, G. E. Swaters, T. S. van den Bremer, and B. R. Sutherland, Propagation and overturning of three-dimensional Boussinesq wavepackets with rotation, Phys. Rev. Fluids **6**, 044801 (2021).

[20] B. R. Sutherland, Finite-amplitude internal wavepacket dispersion and breaking, J. Fluid Mech. **429**, 343 (2001).

[21] G. B. Whitham, A general approach to linear and nonlinear dispersive waves using a Lagrangian, J. Fluid Mech. **22**, 273 (1965).

[22] G. B. Whitham, *Linear and Nonlinear Waves* (Wiley, New York, 1974), p. 636.

[23] V. I. Shrira, On the propagation of a three-dimensional packet of weakly non-linear internal gravity waves, Int. J. Non-Lin. Mech. **16**, 129 (1981).

[24] A. Tabaei and T. R. Akylas, Resonant long-short wave interactions in an unbounded rotating stratified fluid, Stud. Appl. Math. **119**, 271 (2007).

[25] F. P. Bretherton, The propagation of groups of internal gravity waves in a shear flow, Q. J. R. Meteorol. Soc. **92**, 466 (1966).

[26] F. P. Bretherton and C. J. R. Garrett, Wavetrains in inhomogeneous moving media, Proc. R. Soc. London, Ser. A **302**, 529 (1969).

[27] T. J. Dunkerton and D. C. Fritts, Transient gravity wave-critical layer interaction. Part I: Convective adjustment and the mean zonal acceleration, J. Atmos. Sci. **41**, 992 (1984).

[28] D. C. Fritts and T. J. Dunkerton, A quasi-linear study of gravity-wave saturation and self-acceleration, J. Atmos. Sci. **41**, 3272 (1984).

[29] W. Blumen, Reflection of hydrostatic gravity waves in a stratified shear flow. Part I: Theory, J. Atmos. Sci. **42**, 2255 (1985).

[30] S. D. Eckermann, Influence of wave propagation on the Doppler spreading of atmospheric gravity waves, J. Atmos. Sci. **54**, 2554 (1997).

[31] K. M. Huang, S. D. Zhang, and F. Yi, Propagation and reflection of gravity waves in a meridionally sheared wind field, J. Geophys. Res. **113**, D09106 (2008).

[32] K. M. Huang, S. D. Zhang, and F. Yi, Reflection and transmission of atmospheric gravity waves in a stably sheared horizontal wind field, J. Geophys. Res. **115**, D16103 (2010).

[33] C. J. Heale and J. B. Snively, Gravity wave propagation through a vertically and horizontally inhomogeneous background wind, J. Geophys. Res. Atmos. **120**, 5931 (2015).

[34] R. H. J. Grimshaw, The modulation of an internal gravity-wave packet, and the resonance with the mean motion, Stud. Appl. Math. **56**, 241 (1977).

[35] T. R. Akylas and A. Tabaei, Resonant self-acceleration and instability of nonlinear internal gravity wavetrains, in *Frontiers of Nonlinear Physics*, edited by A. Litvak (Institute of Applied Physics, Nizhny Novgorod, Russia, 2005), pp. 129–135.

[36] H. V. Dosser and B. R. Sutherland, Anelastic internal wavepacket evolution and stability, J. Atmos. Sci. **68**, 2844 (2011).

[37] T. R. Robinson, Nonlinear reflection of internal gravity waves by thermospheric winds, Adv. Space Res. **20**, 1261 (1997).

[38] B. R. Sutherland, Internal wave reflection in uniform shear, Q. J. R. Meteorol. Soc. **126**, 3255 (2000).

[39] L. Eberly and B. R. Sutherland, Anelastic internal wave reflection and transmission in uniform retrograde shear, Phys. Fluids **26**, 026601 (2014).

[40] O. Bühler and M. E. McIntyre, On non-dissipative wave-mean interactions in the atmosphere or oceans, J. Fluid Mech. **354**, 301 (1998).

[41] D. C. Fritts, S. L. Vadas, and Y. Yamada, An estimate of strong local body forcing and gravity wave radiation based on OH airglow and meteor radar observations, Geophys. Res. Lett. **29**, 71-1 (2002).

[42] S. M. Smith, S. L. Vadas, W. J. Baggaley, G. Hernandez, and J. Baumgardner, Gravity wave coupling between the mesosphere and thermosphere over New Zealand, J. Geophys. Res. Space Phys. **118**, 2694 (2013).

[43] K. Bossert, C. G. Kruse, C. J. Heale, D. C. Fritts, P. B. Williams, J. B. Snively, P.-D. Pautet, and M. J. Taylor, Secondary gravity wave generation over New Zealand during the DEEPWAVE campaign, J. Geophys. Res. Atmos. **122**, 7834 (2017).

[44] T. P. Lane and R. D. Sharman, Gravity wave breaking, secondary wave generation, and mixing above deep convection in a three-dimensional cloud model, Geophys. Res. Lett. **33**, L23813 (2006).

[45] E. Becker and S. L. Vadas, Secondary gravity waves in the winter mesosphere: Results from a high-resolution global circulation model, J. Geophys. Res. Atmos. **123**, 2605 (2018).

[46] D. C. Fritts, W. Dong, T. S. Lund, S. Weiland, and B. Laughman, Self-acceleration and instability of gravity wave packets: 3. Three-dimensional packet propagation, secondary gravity waves, momentum transport, and transient mean forcing in tidal winds, J. Geophys. Res. Atmos. **125**, 1 (2020).

[47] T. S. Lund, D. C. Fritts, K. Wan, B. Laughman, and H.-L. Liu, Numerical simulation of mountain waves over the Southern Andes. Part I: Mountain waves and secondary wave character, evolutions, and breaking, J. Atmos. Sci. **77**, 4337 (2020).

[48] D. C. Fritts, T. S. Lund, K. Wan, and H.-L. Liu, Numerical simulation of mountain waves over the Southern Andes. Part II: Momentum fluxes and wave–mean-flow interactions, J. Atmos. Sci. **78**, 3069 (2021).

[49] S. L. Vadas and D. C. Fritts, Gravity wave radiation and mean responses to local body forces in the atmosphere, J. Atmos. Sci. **58**, 2249 (2001).

[50] S. L. Vadas and D. C. Fritts, The importance of spatial variability in the generation of secondary gravity waves from local body forces, Geophys. Res. Lett. **29**, 45-1 (2002).

[51] S. L. Vadas, D. C. Fritts, and M. J. Alexander, Mechanism for the generation of secondary waves in wave breaking regions, J. Atmos. Sci. **60**, 194 (2003).

[52] S. L. Vadas and D. C. Fritts, Influence of solar variability on gravity wave structure and dissipation in the thermosphere from tropospheric convection, J. Geophys. Res. **111**, A10S12 (2006).

[53] T. E. Baldock, C. Swan, and P. H. Taylor, A laboratory study of nonlinear surface waves on water, Philos. Trans. R. Soc. A **354**, 649 (1996).

[54] M. L. McAllister, T. A. A. Adcock, P. H. Taylor, and T. S. van den Bremer, The set-down and set-up of directionally spread and crossing surface gravity wave groups, J. Fluid Mech. **835**, 131 (2018).

[55] O. M. Phillips, On the dynamics of unsteady gravity waves of finite amplitude. Part 1. The elementary interactions, J. Fluid Mech. **9**, 193 (1960).

[56] P. Müller, G. Holloway, F. Henyey, and N. Pomphrey, Nonlinear interactions among internal gravity waves, Rev. Geophys. **24**, 493 (1986).

[57] T. Dauxois, S. Joubaud, P. Odier, and A. Venaille, Instabilities of internal gravity wave beams, Annu. Rev. Fluid Mech. **50**, 131 (2018).

[58] A. Eliassen and E. Palm, On the transfer of energy in stationary mountain waves, Geofys. Publ. **22**, 1 (1961).

[59] D. J. Acheson, On over-reflexion, J. Fluid Mech. **77**, 433 (1976).

[60] D. G. Andrews and M. E. McIntyre, Planetary waves in horizontal and vertical shear: The generalized Eliassen–Palm relation and the mean flow acceleration, J. Atmos. Sci. **33**, 2031 (1976).

[61] D. G. Andrews and M. E. McIntyre, On wave action and its relatives, J. Fluid Mech. **89**, 647 (1978).

[62] J. F. Scinocca and T. G. Shepherd, Nonlinear wave-activity conservation laws and Hamiltonian structure for the two-dimensional anelastic equations., J. Atmos. Sci. **49**, 5 (1992).

[63] T. A. Shaw and T. G. Shepherd, Wave-activity conservation laws for the three-dimensional anelastic and Boussinesq equations with a horizontally homogeneous background flow, J. Fluid Mech. **594**, 493 (2008).

[64] N. B. Garnier, A. Chiffaudel, F. Daviaud, and A. Prigent, Nonlinear dynamics of waves and modulated waves in 1D thermocapillary flows. I. General presentation and periodic solutions, Physica D **174**, 1 (2003).

[65] M. J. Mercier, N. B. Garnier, and T. Dauxois, Reflection and diffraction of internal waves analyzed with the Hilbert transform, Phys. Fluids **20**, 086601 (2008).

[66] K. Gregory and B. R. Sutherland, Transmission and reflection of internal wave beams, Phys. Fluids **22**, 106601 (2010).

[67] W. H. Press, S. A. Teukolsky, W. T. Vetterling, and B. P. Flannery, *Numerical Recipes: The Art of Scientific Computing*, 3rd ed. (Cambridge University Press, New York, 2007), p. 1235.

[68] B. R. Sutherland, W. Reeves, and T. S. van den Bremer, Flows induced by Coriolis-influenced vertically propagating two-dimensional internal gravity wave packets, Phys. Rev. Fluids **5**, 064805 (2020).

[69] J. H. Williamson, Low-storage Runge–Kutta schemes, J. Comput. Phys. **35**, 48 (1980).

[70] D. R. Durran, *Numerical Methods for Fluid Dynamics*, 2nd ed. (Springer-Verlag, New York, 2010), p. 516.

[71] Digital Research Alliance of Canada, www.alliancecan.ca.

[72] P. Godon and G. Shaviv, A two-dimensional time dependent Chebyshev method of collocation for the study of astrophysical flows, Comput. Methods Appl. Mech. Eng. **110**, 171 (1993).

[73] C. J. Subich, K. G. Lamb, and M. Stastna, Simulation of the Navier–Stokes equations in three dimensions with a spectral collocation method, Int. J. Numer. Meth. Fluids **73**, 103 (2013).

[74] See Supplemental Material at http://link.aps.org/supplemental/10.1103/PhysRevFluids.7.114802 for additional information in the form of supplementary movies.

[75] G. S. Voelker, T. R. Akylas, and U. Achatz, An application of WKBJ theory for triad interactions of internal gravity waves in varying background flows, Q. J. R. Meteorol. Soc. **147**, 1112 (2021).

[76] B. Voisin, Internal wave generation in uniformly stratified fluids. Part 1. Green's function and point sources, J. Fluid Mech. **231**, 439 (1991).

[77] B. Voisin, Internal wave generation in uniformly stratified fluids. Part 2. Moving point sources, J. Fluid Mech. **261**, 333 (1994).

[78] J. Muraschko, M. D. Fruman, U. Achatz, S. Hickel, and Y. Toledo, On the application of Wentzel–Kramer–Brillouin theory for the simulation of the weakly nonlinear dynamics of gravity waves, Q. J. R. Meteorol. Soc. **141**, 676 (2015).

[79] J. Bowman and A. Hammerlindl, Asymptote: A vector graphics language, TUGboat: Commun. TeX Users Group **29**, 288 (2008).

[80] K. M. Thyng, C. A. Greene, R. D. Hetland, H. M. Zimmerle, and S. F. DiMarco, True colors of oceanography: Guidelines for effective and accurate colormap selection, Oceanography **29**, 9 (2016).